


Charging mechanisms and orbital dynamics of charged dust grains in the LHC

P. Bélanger^{1,2}, R. Baartman², G. Iadarola¹, A. Lechner¹, B. Lindstrom¹,
R. Schmidt¹ and D. Wollmann¹

¹CERN, 1211 Geneva 23, Switzerland

²TRIUMF, 4004 Wesbrook Mall, Vancouver, BC, V6T 2A3, Canada

 (Received 14 May 2021; revised 1 August 2022; accepted 6 September 2022; published 13 October 2022)

Dust grains interacting with the beam of particle accelerators are believed to be the cause of several detrimental effects such as beam losses, emittance growth, pressure bursts, and even quenches of superconducting magnets. Experimental observations suggest that these grains are positively charged in electron storage rings and negatively charged in the Large Hadron Collider (LHC). In this paper, the charging mechanisms for dust grains in the LHC are discussed and a possible explanation for the observed polarity is presented. Electron collection, secondary electron emission, and photoelectric emission are considered because of the presence of electron clouds and synchrotron radiation. It is found that the same mechanisms can explain both the positive grain polarity observed in electron storage rings and the negative polarity in the LHC. As a consequence of the charge acquired, the possibility of grains orbiting the beam is discussed. The orbital dynamics in a logarithmic potential is analyzed and critical parameters for describing such orbits are introduced. Finally, LHC beam losses attributed to beam-dust interactions with multiple loss peaks are presented. It is shown that they have an amplitude and a peak separation consistent with what can be expected for orbiting grains.

DOI: [10.1103/PhysRevAccelBeams.25.101001](https://doi.org/10.1103/PhysRevAccelBeams.25.101001)

I. INTRODUCTION

Micrometer-sized dust particulates, made of fine grains of solid matter, are known to have caused intensity drops in electron storage rings (TRISTAN, CESR, HERA, and DORIS) [1–3], pressure bursts in the SuperKEKB positron storage ring [4], and sporadic beam losses as well as quenches of superconducting magnets in the LHC [5–7]. The presence of contaminants in the vacuum chamber of modern accelerators is not fully understood and seems unavoidable, even with careful cleaning measures [8]. It is possible that solid dust grains are created by the flaking or sputtering of the inner walls of the chamber with time.

However, in the case of the LHC, experimental observations suggest that dust was introduced during the assembly of the LHC. Since it is likely that dust contamination will also occur in the High Luminosity upgrade of the LHC (HL-LHC) and future accelerators such as the Future Circular Collider (FCC), the conditions leading to the interaction of dust grains with the beam, and more precisely the charging of dust grains, need to be investigated.

Recent studies on the dynamics of beam-dust interactions in the LHC reported strong evidence that the grains that interact with the LHC beam are generally negatively charged [9,10]. This observation is the main motivation for this paper, where a first model for dust charging mechanisms in particle accelerators is proposed.

In the first half of this paper, the net charge of dust grains subject to several charging and discharging currents is discussed. It is found that dust grains in the LHC are expected to acquire a negative charge and that dust grains in negative-particle accelerators can acquire a negative or positive charge. As a consequence of this accumulated charge, dust grains can be attracted by the beam and interact with it or orbit around it.

The second half of this paper proposes a theoretical description of the dynamics of such a system, where charged grains orbit a beam of particles. Following up on several theoretical studies on the dynamics of charged dust grains in the LHC [9,11–13], their interaction with the beam and the resulting beam losses are also discussed. Simulations of the expected beam losses are compared to measurements in the LHC.

II. DUST IN THE LHC

Throughout LHC Run I (2009–2013) and Run II (2015–2018), tens of thousands of beam loss events have been attributed to isolated dust grains interacting with the LHC

Published by the American Physical Society under the terms of the Creative Commons Attribution 4.0 International license. Further distribution of this work must maintain attribution to the author(s) and the published article's title, journal citation, and DOI.

proton beam. These events, referred to as unidentified falling objects (UFOs) in the LHC, are characterized by beam losses lasting up to a few milliseconds with an asymmetric Gaussian profile.

The prevailing hypothesis to explain this phenomenon is that dust grains fall from the top of the beam screen and enter the vicinity of the beam, where they are ionized and eventually repelled [5,6,11]. These events happen at a rate of a few occurrences per hour of stable beams [14], all along the accelerator, with no known release mechanism.

From energy deposition studies [15] and dust collection in sections of the accelerator [7,16], the size of the grains leading to observable beam losses is believed to be in the order of 1–100 μm . The precise composition of the contaminants is not known, although metallic and ceramic components have been found. To explain the time profile of beam losses, in particular, the fast rise times of the beam losses observed with beam loss monitors, it has been shown that an initial charge is required on the grains [9,10]. Charging mechanisms to explain this observation are discussed in the coming sections.

III. CHARGING OF DUST GRAINS

Outside of accelerators, the interaction of dust grains with free charges or ionized gases is the subject of a field of its own, generally referred to as *Dusty Plasma*. Since the observation of the so-called Lunar Horizon-Glow on the surface of the Moon in 1974, it is known that dust grains can accumulate a charge sufficient to be lifted by electric fields in the order of a few kV/m [17]. Later on, dust dynamics and dust charging have been the subject of numerous studies to understand the formation of planet surfaces [18,19], the formation of cosmic plasmas [20], and to mitigate the undesirable effect of dust in vacuum environments and clean rooms (e.g., in the microelectronics industry). Exhaustive reviews on the status of the field can be found in Mendis [21] or Piel [22].

Despite the variety of environments where dust is found to be charged, the processes responsible for the charging are similar. These processes are driven by an electric contact between different surfaces, the presence of free charges, the presence of high energy photons, and/or the presence of electromagnetic fields. In this regard, particle accelerators offer favorable conditions for the dust to become charged. The main charging mechanisms acting on a single dust grain are [21,23]:

Induction and contact charging, where electrons move between a conductive surface and the dust grain when a physical contact is established. The direction of the charging current depends on the background electric field and the electron affinity of both materials.

Electron collection, where incoming low energy electrons are captured in the bulk of the grain. This mechanism leads to a negative charging current.

Secondary electron emission (SEE), where particles, typically other electrons, deposit energy in the bulk of the grain and excite secondary electrons which then escape the dust grain. This mechanism leads to a positive charging current.

Photoelectric emission, where photons excite electrons that escape the grain due to the photoelectric effect. This mechanism leads to a positive charging current.

Thermionic emission, where electrons spontaneously leave the grain due to their high thermal energy. This mechanism is generally considered for temperatures above 1000 K and leads to a positive charging current.

Field emission, where electrons spontaneously leave the grain due to a high negative potential inside of it. This mechanism leads to a positive charging current and dictates the maximum charge that can be carried by a dust grain.

In general, the total charging current on a single dust grain is the sum of several currents from the list presented. All the charging mechanisms scale with the surface potential of the grain, Φ , since it eventually prevents charges from entering or exiting the dust grain. For a spherical grain, the potential is

$$\Phi = \frac{Q}{4\pi\epsilon_0 R}, \quad (1)$$

where ϵ_0 is the vacuum permittivity, Q is the total charge carried by the grain, and R , its radius.

For positive and negative charging currents, the magnitude of the current tends to decrease as the accumulated charge becomes more positive or negative, respectively. As such, there is a surface potential for which there is no net current, called the equilibrium surface potential, Φ_{eq} . In practice, micrometer-sized dust grains in diverse environments (from laboratory plasmas to the rings of Saturn [19,21]) are found to carry charges of $10^0 e$ to $10^6 e$, where e is the elementary charge. This leads to surface potentials of 10^{-5} V to 10^3 V and charge-to-mass ratios, Q/m , of 10^{-12} to 10^1 C/kg.

Whereas Φ is the critical quantity driving most charging mechanisms, the charge-to-mass ratio is the critical quantity driving the dynamics of charged grains and will be important in the second half of this paper. The former varies following $\Phi \propto R^{-1}$ and the latter varies following $Q/m \propto R^{-3}$. Table I shows a cross-reference comparison of the order of magnitude to expect for each quantity.

TABLE I. Comparison of the order of magnitude for the charge Q , the surface potential Φ , and the charge-to-mass ratio Q/m of a copper grain.

Q (C)	Φ (V)		Q/m (C/kg)	
	$R = 5 \mu\text{m}$	$R = 50 \mu\text{m}$	$R = 5 \mu\text{m}$	$R = 50 \mu\text{m}$
$1e$	2.9×10^{-4}	2.9×10^{-5}	3.4×10^{-8}	3.4×10^{-11}
$10^3 e$	2.9×10^{-1}	2.9×10^{-2}	3.4×10^{-5}	3.4×10^{-8}
$10^6 e$	2.9×10^2	2.9×10^1	3.4×10^{-2}	3.4×10^{-5}
$10^9 e$	2.9×10^5	2.9×10^4	3.4×10^1	3.4×10^{-2}

In almost all natural conditions, dust is found to carry a negative charge [19,21–23]. In principle, secondary electron emission, photoelectric emission, and thermionic emission could all lead to a positively charged grain. However, unless the grain is perfectly isolated in space with no neighboring surfaces in its vicinity [24,25], electrons emitted from the surroundings are collected by the grain and, in most cases, lead to a net negative charge at equilibrium. This was confirmed experimentally by illuminating an accumulation of dust grains with UV light, which resulted in negatively charged grains on the top layer [18,19].

For submicron grain sizes, the conditions to obtain positively charged dust grains are made easier by a significant increase in the secondary electron yield due to geometrical reasons [26]. However, in presence of low temperature plasma, dust grains are always found to carry a negative charge [21]. Finally, if contact charging is the only mechanism at play, the polarity can either be positive or negative, depending on the materials and the orientation of the background electric field.

In the following sections, the charging mechanisms listed above are applied to the case of the LHC and numerical calculations for the equilibrium potential are presented. The case of electron storage rings is also discussed. Thermionic emission is omitted from the discussion, as it is negligible at low temperatures. Field emission is also omitted, as it becomes important for surface potentials of $-10^8 \text{ V/m} \times R$ to $-10^9 \text{ V/m} \times R$ [23] which is higher than the equilibrium surface potential found in the coming sections.

A. Induction and contact with the beam screen

When a dust grain is lying on a conductive substrate, charges can move from the substrate to the grain and vice versa. Assuming a perfectly conductive contact, the grain would discharge into the substrate, overcoming all other charging currents and eventually reaching an electrically neutral state. If an additional background electric field E_{BG} is present, the dust grain charges to a nonzero surface potential, Φ_{ind} , due to electric induction. The induced surface potential follows [27]:

$$\Phi_{\text{ind}} = -\frac{\pi^2}{18} \left(\frac{3\epsilon_r}{\epsilon_r + 2} \right) R \times E_{\text{BG}} \quad (2)$$

where $\frac{3\epsilon_r}{\epsilon_r + 2}$ is the Pauthenier's coefficient and ϵ_r is the relative permittivity of the dust grain. E_{BG} is positive when the electric field is oriented from the dust grain toward the conductive surface and negative otherwise.

In the LHC, the beam screen acts as the conductive substrate, and the direction of the beam's electric field is such that electrons are pulled from the beam screen into the grain. For the nominal beam intensity of the LHC, $2808 \times 1.15 \times 10^{11}$ protons, E_{BG} is in the order of a few kV/m and the expected Φ_{ind} for micrometer-sized grains is in the

order of -1 to -200 mV. Hence, in the limit of a perfectly conductive contact with the beam screen, the net charge acquired by a dust grain in a particle accelerator is fixed by the background electric field and the polarity is opposite to the one of the beam.

However, the electrical contact between dust grains and a planar surface is rarely perfect and one can assume that a capacitance, e.g., coming from an oxide layer, separates the grain from the substrate. The time constant for such a system to reach an equilibrium is generally in the order of ms [28] and depends on the precise nature of the electrical contact, which can be described by an effective charging resistance R_c and an effective capacitance C_c . With these assumptions, the charging or discharging current density due to the contact with the beam screen follows [28]:

$$\begin{aligned} J_{\text{ind}}(\Phi) &= \frac{1}{\pi R^2} \frac{4\pi\epsilon_0 R}{C_c R_c} [\Phi_{\text{ind}} - \Phi] \\ &= \frac{1}{\pi R^2} \frac{1}{2\epsilon_{r,\text{ox}}} \left(\frac{\sigma_{\text{ox}} A_c}{\ell_{\text{ox}}} \right) [\Phi_{\text{ind}} - \Phi] \quad (3) \end{aligned}$$

where A_c is the contact area between the surfaces, σ_{ox} is the conductivity of the oxide layer, ℓ_{ox} is the thickness of the oxide layer, and $\epsilon_{r,\text{ox}}$ is its relative permittivity.

The current density in Eq. (3) is averaged over the cross section of the grain ($1/\pi R^2$) to be consistent with the current densities presented in the following sections. Due to the low contact area between a spherical dust grain and a planar surface, the charging resistance $R_c = \ell_{\text{ox}}/(\sigma_{\text{ox}} A_c)$ can be in the order of several thousands of $G\Omega$.

Assuming a 1-nm alumina layer with a conductivity between 10^{-16} and 10^{-12} S/m, a relative permittivity of 10, and a contact area of about 1% of the cross section of the grain [28], one finds a current density between $J_{\text{ind}} \sim 10^{10} \text{ e}^- \text{ s}^{-1} \text{ m}^{-2}$ and $J_{\text{ind}} \sim 10^{14} \text{ e}^- \text{ s}^{-1} \text{ m}^{-2}$ at $\Phi = -100 \text{ V}$.

As will be seen in the following sections, this discharging current is many orders of magnitude smaller than the charging currents coming from the interaction of the grain with electron clouds and synchrotron radiation ($\sim 10^{19} \text{ e}^- \text{ s}^{-1} \text{ m}^{-2}$). Hence, assuming that the electrical contact between the dust grain and the beam screen is not perfectly conductive, the discharging current in the beam screen can be neglected.

B. Charging from electron clouds

Observations at the positron ring of SuperKEKB [29] showed that dust grains entering the beam caused very intense beam losses leading to collimator damage. It was demonstrated that an attractive force increases the probability of interaction between dust grains and the beam, which indicates that dust grains are likely to be negatively charged. Terui *et al.* [29] argue that the charging occurs when a free-falling dust grain passes through the electron cloud of SuperKEKB. It is believed that a similar effect

takes place in the LHC, where the electron cloud plays an important role in the charging of dust grains, as discussed below.

1. Electron cloud formation

The beam parameters of the LHC, specifically the number of bunches, the bunch intensity, and the bunch spacing offer conditions that allow for the buildup of electron clouds. Electrons can primarily be generated in the beam chamber by a number of processes, e.g., ionization of residual gas and photoelectric emission from synchrotron radiation. Their number, however, can exponentially increase via a beam-induced multipacting mechanism and lead to the formation of the so-called electron clouds.

Beam-induced multipacting, driven by the electric field of successive bunches (first observed in the ISR proton-proton storage ring [30]) arises from the resonant motion of electrons bouncing back and forth between opposite walls of the vacuum chamber [31]. The number of secondary electrons released after the impact of one electron on the chamber wall, called the secondary electron yield (SEY), is a function of the energy of the impacting electrons. Since the SEY is larger than unity for most electrons involved in the multipacting mechanism, the secondary electrons outnumber the primaries, and a cloud builds up.

Because of internal repulsive forces, the electron density eventually reaches a saturation point. Under stable conditions, the electron density in the beam pipe of the LHC can be in the order of 10^{12} e^-/m^3 [31,32]. Most electrons are concentrated near the surface of the beam screen, rather than in the center of the pipe. During the passage of a bunch, electrons can either receive a single kick or oscillate around the bunch, depending on their position. As a result, most of the electrons accelerated by the beam are sent to the beam screen, after the passage of the bunch, with an energy of $k_B T_e \sim 0\text{--}2000$ eV [33], where T_e is their temperature and k_B is the Boltzmann constant.

All of these electrons are then either absorbed or contribute to new secondaries, which leave the surface of the beam screen with a low energy of about $k_B T_e \sim 1\text{--}10$ eV [33], independently of the energy of the primaries. For this reason, close to the surface of the beam screen, the energy spectrum of the cloud is dominated by low energy electrons [34]. This observation is important for the numerical evaluation of the net charge acquired by a dust grain under those conditions, as will be seen in the following sections.

2. Secondary electron yield

As mentioned, when electrons impact a surface (be it the chamber wall or a dust grain), the secondary electron yield, $\delta(E)$, is a function of the energy of the incoming electrons. In general, the yield also depends on the surface roughness, the surface temperature, and the incoming incidence angle,

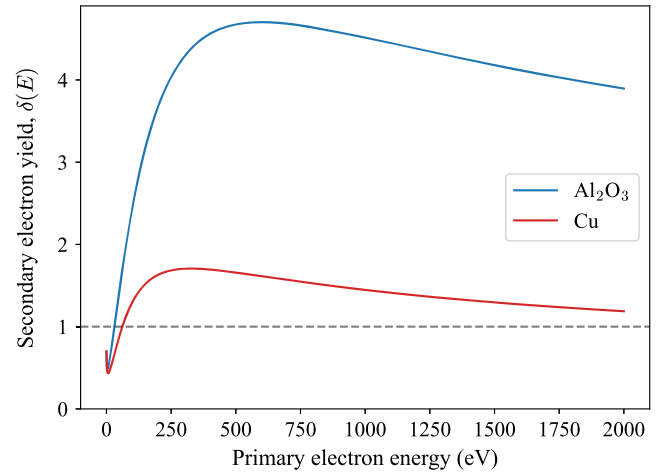


FIG. 1. Secondary electron yield curves of copper with $\delta_{\max} = 1.7$ at $E_{\max} = 332$ eV and alumina with $\delta_{\max} = 4.7$ at $E_{\max} = 600$ eV [35].

but these small corrections are neglected in the context of this paper.

An example of the total secondary electron yield as a function of the primary electron energy is shown in Fig. 1 for Cu and Al_2O_3 grains. For primary electrons of low energy, all materials have $\delta(E) < 1$ and tend to either collect the electrons or elastically reflect them. With increasing energy, $\delta(E)$ values exceed 1 over a certain range of energies, depending on the material. The total effect can be expressed as the sum of the true electron yield and the yield of elastically reflected electrons: $\delta(E) = \delta_{\text{true}}(E) + \delta_{\text{elas}}(E)$.

The true SEY follows an almost universal curve [26] characterized by two material parameters, the maximum yield δ_{\max} and the energy at which this maximum occurs, E_{\max} :

$$\delta_{\text{true}}(E) = \delta_{\max} \times \frac{s_{\delta} \left(\frac{E}{E_{\max}}\right)}{s_{\delta} - 1 + \left(\frac{E}{E_{\max}}\right)^{s_{\delta}}} \quad (4)$$

where $s_{\delta} = 1.35$ is an empirical value [36]. The contribution of elastically scattered electrons is mainly noticeable at low energy and follows:

$$\delta_{\text{elas}} = R_0 \left(\frac{\sqrt{E} - \sqrt{E + E_{\text{elas}}}}{\sqrt{E} + \sqrt{E + E_{\text{elas}}}} \right)^2, \quad (5)$$

where E_{elas} and R_0 are two other material parameters. For the numerical estimates of Sec. III D, $R_0 = 0.7$ and $E_{\text{elas}} = 150$ eV will be used, assuming that dust grains in the LHC have the same composition as the beam screen surface [36,37] and are made of copper.

3. Collection and secondary electron current

Consider a dust grain lying on the surface or in the vicinity of the beam screen of the LHC, as illustrated in

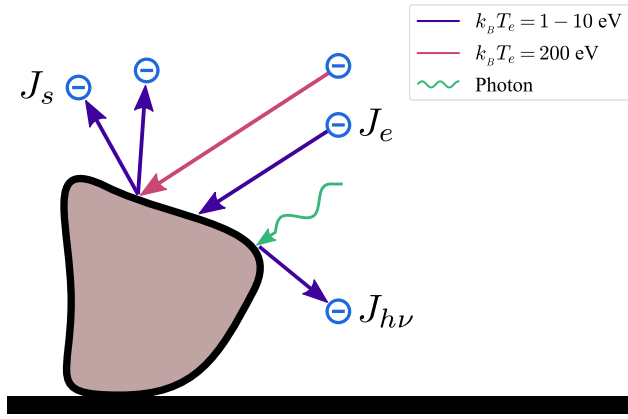


FIG. 2. Representation of a dust grain on the surface of the beam screen. The grain is bombarded by electrons from the surrounding electron cloud. Electrons with an energy of a few eV remain in the dust grain (negative charging current density J_e). Electrons with an energy of a few 100 eV excite secondary electrons leaving the dust grain (positive charging current density J_s). The grain is also bombarded by photons from the synchrotron radiation, leading to the positive photoelectric emission current density $J_{h\nu}$.

Fig. 2. Due to the surrounding electron cloud, the grain is constantly bombarded by electrons. Low energy electrons entering the bulk of the grain will be absorbed, contributing to a negative charging current due to the collection current density J_e .

On the other hand, by the same mechanism responsible for the formation of electron clouds, electrons of a few hundred eV will excite secondaries in the grain and contribute to a positive charging current from the SEE current density J_s . Analytical expressions for the charging current densities can be obtained assuming that the incoming electrons follow a Maxwellian energy distribution with a characteristic temperature T_e . The resulting current densities have been previously calculated by Meyer-Vernet [38] and Chow [26]. Their results are summarized below for completeness. The collection current density and secondary electron current density scale with a common amplitude parameter, J_0 , are given by

$$J_0(n_e, T_e) = en_e \left(\frac{k_B T_e}{2\pi m_e} \right)^{1/2}, \quad (6)$$

where n_e is the number of electrons per unit volume and m_e is the electron mass. The collection current density J_e on a dust grain with a surface potential Φ is

$$J_e(\Phi, n_e, T_e) = -J_0 \times \begin{cases} \exp\left(\frac{e\Phi}{k_B T_e}\right) & \text{for } \Phi < 0 \\ \left(1 + \frac{e\Phi}{k_B T_e}\right) & \text{for } \Phi \geq 0. \end{cases} \quad (7)$$

For the secondary electron current density J_s , the SEY $\delta(E)$ has to be taken into account, which leads to

$$J_s(\Phi, n_e, T_e) = J_0 \frac{\exp\left(\frac{e\Phi}{k_B T_e}\right)}{(k_B T_e)^2} \eta(\Phi) \quad (8)$$

where:

$$\eta(\Phi) = \begin{cases} I_\delta(0) & \text{for } \Phi < 0 \\ I_\delta(e\Phi) \exp\left(-\frac{e\Phi}{k_B T_s}\right) \left(1 + \frac{e\Phi}{k_B T_s}\right) & \text{for } \Phi \geq 0 \end{cases} \quad (9)$$

with:

$$I_\delta(e\Phi) = \int_{e\Phi}^{\infty} E \delta(E) \exp\left(-\frac{E}{k_B T_e}\right) dE, \quad (10)$$

where T_s is the characteristic temperature of secondary electrons emitted from the dust grain. For a Maxwellian distribution, $k_B T_s \approx 3$ eV gives an appropriate distribution for secondary electrons of most materials [26].

The balance of these currents mainly depends on the SEY of the grain. For submicrometer-sized grains, the SEY can be many times higher than the one of the materials itself due to geometrical reasons. However, for grain radii above $\sim 1 \mu\text{m}$, this effect can be neglected and the SEY of the grain follows the one of an infinite planar slab [26] shown in Fig. 1.

C. Photoelectric emission

As illustrated in Fig. 2, photons are also present in the beam pipe of storage rings due to synchrotron radiation. Photons impinging on a dust grain with an energy above the work function W_f of the material will release photoelectrons, leading to an additional positive charging current. For most materials, $W_f \sim 5$ eV, which is lower than the typical energy of synchrotron radiation (0–1000 eV for the LHC at 6.5 TeV).

The total power P_{tot} of synchrotron radiation produced in a length L of the bending magnets of a storage ring follows [39]:

$$P_{\text{tot}} = \frac{L}{2\pi\rho} \left[\frac{e^2}{4\pi\epsilon_0} \left(\frac{2c\gamma^4}{3\rho^2} \right) \right] N_p, \quad (11)$$

where c is the speed of light in vacuum, γ is the Lorentz factor of the accelerated particles, ρ is the bending radius, and N_p is the number of particles in the beam. The average energy $\langle h\nu \rangle$ of these photons is given by

$$\langle h\nu \rangle = \frac{8\sqrt{3}}{45} \left(\frac{3c\gamma^3}{2\rho} \right) \hbar \quad (12)$$

where $\hbar = \frac{h}{2\pi}$ is the reduced Planck constant and ν is the photon frequency. As a result, the total rate of photons per unit area $\dot{\Gamma}_{\text{tot}}$ collected on a surface S of the beam screen is

$$\dot{\Gamma}_{\text{tot}} = \frac{1}{S} \frac{P_{\text{tot}}}{\langle h\nu \rangle}. \quad (13)$$

In the LHC, there is an azimuthal dependence on the distribution of synchrotron radiation irradiating the beam screen because of the presence of sawtooth absorbers on the outer side of the bent sections [40]. To remain general, this azimuthal dependence will be neglected for the moment and the synchrotron radiation will be assumed to uniformly irradiate the surface of the beam screen.

As mentioned, only photons with an energy higher than the work function of the material can lead to photoelectrons. By numerically integrating the synchrotron radiation spectrum [39,41], one can show that the fraction of photons with sufficient energy ($h\nu > 5$ eV) is $\dot{\Gamma}_{\text{eff}} \approx 0.33\dot{\Gamma}_{\text{tot}}$ for the LHC.

When bombarding a dust grain, these photons are the ones responsible for the photoelectric emission current density $J_{h\nu}(\Phi)$. If the grain is positively charged, photoelectrons have to overcome an additional coulomb potential and $J_{h\nu}(\Phi)$ is reduced. For neutral or negatively charged dust grains, the charging current reaches a saturation value:

$$J_{h\nu}^{\text{sat}} = e\dot{\Gamma}_{\text{eff}}Q_{h\nu}\delta_{h\nu}, \quad (14)$$

which scales with the photoelectric yield $\delta_{h\nu}$, the photon absorption efficiency $Q_{h\nu}$, and the photon rate. The photoelectric yield is taken to be $\delta_{h\nu} = 0.3$ as it is generally in the range of 10%–30% for micrometer-sized grains of most materials [23,42]. For the absorption efficiency, $Q_{h\nu} \approx 1$ for $2\pi R\nu/c > 1$, which is always the case for micrometer-sized grains and photons above the work function of the material.

Following Shukla and Mamun [43], the photoelectric emission current density can be written as

$$J_{h\nu}(\Phi) = \begin{cases} J_{h\nu}^{\text{sat}} & \text{for } \Phi < 0 \\ J_{h\nu}^{\text{sat}} \exp\left(-\frac{e\Phi}{k_B T_{h\nu}}\right) & \text{for } \Phi \geq 0 \end{cases}, \quad (15)$$

where $k_B T_{h\nu}$ is the average energy of the photoelectrons, given by $k_B T_{h\nu} = \langle h\nu \rangle - W_f \approx 5.8$ eV for the case of the LHC at 6.5 TeV.

D. Numerical evaluation of the surface potential

1. LHC

In order to numerically evaluate the charging currents presented in the two previous subsections, the operational LHC parameters are used, namely beam energy of 6.5 TeV and beam intensity of $N_p = 2808 \times 1.15 \times 10^{11}$ protons. From Eq. (13), one finds an average photon rate of $\dot{\Gamma}_{\text{tot}} \sim 1 \times 10^{18}$ photons $\text{s}^{-1} \text{m}^{-2}$ distributed over the full surface of the LHC beam screen, assuming that the photons originate from the eight arc sections of the LHC with a bending radius of $\rho = 2804$ m.

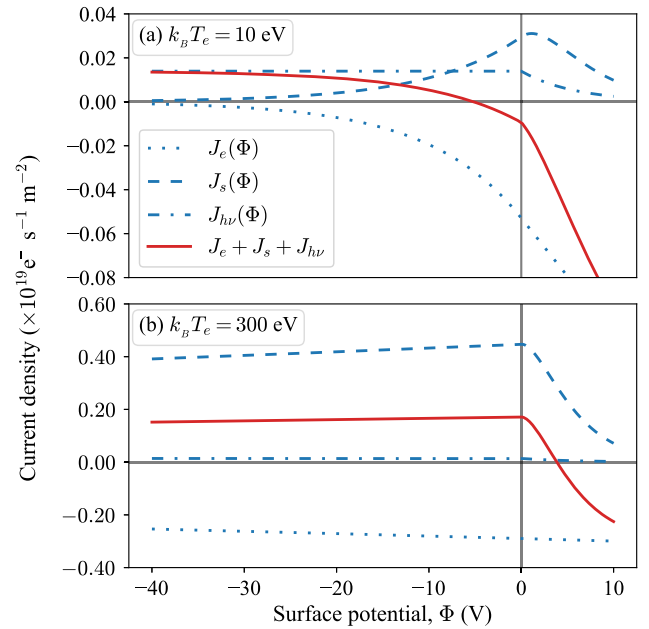


FIG. 3. Charging currents in the LHC for electrons impinging on a Cu dust grain with an energy of (a) 10 eV (b) 300 eV. The photoelectric emission current is independent of the electron cloud and is computed assuming $\dot{\Gamma}(h\nu > 5 \text{ eV}) = 0.33 \times 10^{18} \text{ s}^{-1} \text{m}^{-2}$ photons. The equilibrium potential corresponds to the potential where the net current is $J_e + J_s + J_{h\nu} = 0$.

Figure 3 shows the three charging current densities discussed in the previous sections as well as the net total current density $J_e + J_s + J_{h\nu}$ for two-electron distributions with $k_B T_e = 10$ eV and $k_B T_e = 300$ eV. The dust grain is assumed to be made of copper, with SEY parameters identical to the ones of the beam screen [37]. The stationary condition $J_e + J_s + J_{h\nu} = 0$, where the total current density crosses the axis, is of particular interest since it corresponds to the equilibrium potential Φ_{eq} acquired by a dust grain in those conditions. Because of the high mobility of electrons, this equilibrium state can be reached in the order of nanoseconds for small Φ_{eq} . As one can see, with a fixed photoelectric emission current density, the equilibrium potential varies substantially with the energy of incoming electrons and can either be negative [Fig. 3(a)] or positive [Fig. 3(b)].

The dependence of Φ_{eq} on the energy of incoming electrons, the electron cloud density, and the beam intensity is shown in Fig. 4 for a Cu grain. As one can see, a positive equilibrium potential is found for electron energies above 40 eV, where the SEY of the grain is close to or larger than 1 (see Fig. 1). For electrons of lower energy, which are predominant near the surface of the beam screen, the equilibrium potential becomes negative in conditions where the photoelectric effect is reduced, i.e., for a lower beam intensity. As a general conclusion, when $\delta(E) < 1$, the equilibrium potential becomes more negative with increasing n_e and more positive with increasing $\dot{\Gamma}_{\text{tot}} \propto N_p$.

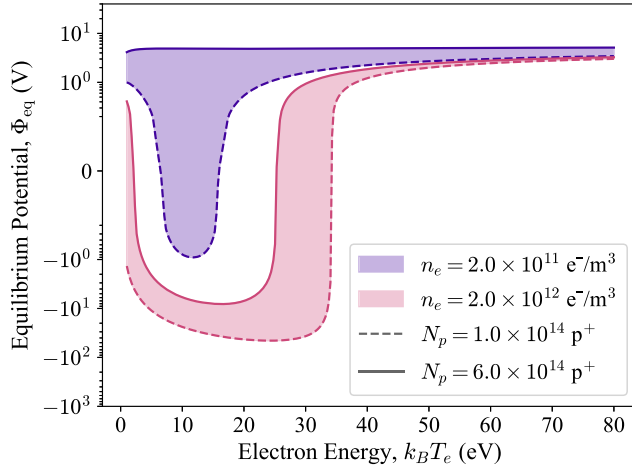


FIG. 4. Equilibrium potential of a Cu grain for beam intensities ranging from $1 \times 10^{14} \text{ p}^+$ to $6 \times 10^{14} \text{ p}^+$, as a function of the energy of the incoming electrons. The results are shown for two-electron cloud densities. The collection and secondary electron currents increase with n_e , whereas the photoelectric current increases with N_p .

In fact, by combining Eqs. (7), (8), and (15) in the equilibrium condition $J_e + J_s + J_{h\nu} = 0$, one can see that the ratio of the number of impinging electrons to the number of impinging photons is of particular interest in order to determine the equilibrium potential at low electron energy [where $\delta(E) < 1$]. Figure 5 shows the dependence of the equilibrium potential on the dimensionless density ratio $\frac{n_e}{\dot{\Gamma}_{\text{eff}}/c}$ for a Cu grain. For a high ratio, electron collection dominates and Φ_{eq} is negative, whereas for a low ratio, the photoelectric emission dominates and Φ_{eq} is positive.

In the LHC, with n_e in the order of $10^{12} \text{ e}^-/\text{m}^3$ and $\dot{\Gamma}_{\text{eff}}$ in the order of $0.33 \times 10^{18} \text{ s}^{-1} \text{ m}^{-2}$ photons, the density ratio is in the order of $\frac{n_e}{\dot{\Gamma}_{\text{eff}}/c} \sim 1 \times 10^3$. Based on Fig. 5, for an electron spectrum dominated by low energy electrons, the equilibrium potential is in the order of -10 V . However, as mentioned previously, the photon rate considered for this calculation ignores the sawtooth pattern on the side of the LHC beam screen, which can reduce $\dot{\Gamma}$ by a factor of 10^4 [40]. In that case, the density ratio can go up to $\frac{n_e}{\dot{\Gamma}/c} \sim 1 \times 10^7$, which leads to an equilibrium potential in the order of -100 V .

Since the SEY is material-independent for low energy electrons, the equilibrium potential shown in Fig. 5 remains valid for grain materials other than Cu. These results are summarized in Table II, along with the corresponding charge-to-mass ratio of the grain. Given the LHC density ratio, the expected charge-to-mass ratio is in the order of -10^{-2} to -10^{-3} C/kg for Cu dust grains of $5 \mu\text{m}$ radius. This result is consistent with previous studies comparing simulated and measured beam losses in the LHC, where the

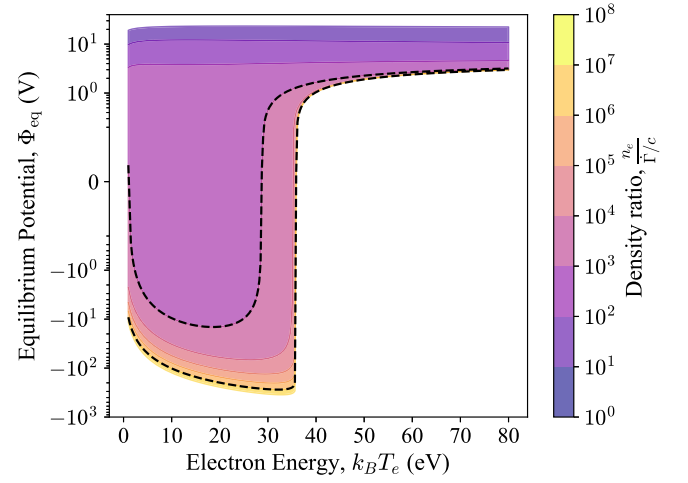


FIG. 5. Equilibrium potential of a Cu grain as a function of the energy of the incoming electrons. The color gradient shows the results for several density ratios. The black dashed lines identify the region corresponding to LHC conditions.

best agreement for Cu grains was found for $-10^{-1} \leq Q/m \leq -10^{-3}$ and $R \leq 22 \mu\text{m}$ [10].

The equilibrium potential of a dust grain depends on a number of parameters. A range of equilibrium potential was computed to account for the fact that the exact conditions inside the beam chamber are not homogeneous. The density of the electron cloud depends on the longitudinal and transversal position on the beam screen, as well as on the magnetic fields present. Additionally, the photon rate from the synchrotron radiation also depends on the local geometry of the beam chamber. Moreover, the material parameters considered can also be changed, since the exact composition of the grains is not precisely known.

As observed in other experiments [18,19], photons hitting surfaces in the vicinity of the dust grain lead to the emission of low energy electrons that will impinge on the grain and contribute to its charging. In that situation, the numerical example presented above shows that for a wide range of parameters, dust grains in the LHC are expected to be negatively charged.

TABLE II. Equilibrium potential and charge-mass-ratio for three density ratios and $k_B T_e = 10 \text{ eV}$. Cu grains with radii of $5\text{--}50 \mu\text{m}$ are considered. The last two rows correspond to the density ratios expected in the LHC.

$\frac{n_e}{\dot{\Gamma}/c}$	$\Phi_{\text{eq}} \text{ (V)}$	$Q/m \text{ (C/kg)}$	
		$R = 5 \mu\text{m}$	$R = 50 \mu\text{m}$
10^1	$+1 \times 10^1$	$+1 \times 10^{-3}$	$+1 \times 10^{-5}$
10^3	-1×10^1	-1×10^{-3}	-1×10^{-5}
10^7	-1×10^2	-1×10^{-2}	-1×10^{-4}

2. Electron storage rings

Besides their impact in the LHC and positron storage rings, dust grains are known to become trapped by electron [1,44] and antiproton [45] beams. In negative-particle accelerators, dust grains can remain in the vicinity of the beam for a long period, causing important intensity loss or emittance growth. Direct [1,46,47] and indirect [2] observations have shown that dust grains can be lifted from the surface of the beam pipe before being trapped. From these observations, it is apparent that dust in electron storage rings can acquire an initial positive charge. This is contrary to the LHC, where the initial charge is negative, as shown above.

For negative-particle beams, a repulsive coulomb force keeps free electrons near the wall of the chamber, where they are reabsorbed without triggering a significant number of secondary electrons. As a result, the electron cloud densities are several orders of magnitude lower than what is found in positive-particle accelerators [48]. This consideration reveals how the charging mechanisms presented in this paper can equally be applied to the case of electron storage rings to explain most historical dust trapping phenomena. Based on experimental measurements of electron cloud densities in the CESR electron-positron storage ring [49], one can compute that the density ratio from the positron beam is around ~ 10 . For the electron beam, subject to the same conditions, the density ratio is much lower due to an important reduction in the electron cloud density. As can be seen from Fig. 5 and Table II, the equilibrium potential of a dust grain under these conditions is expected to be positive and could therefore become trapped by the electron beam. The general conclusion for electron storage rings is that photoelectric emission is expected to dominate [50], which leads to a low density ratio and the accumulation of a net positive charge on dust grains.

IV. ORBITING DUST GRAINS IN THE LHC

As shown in previous sections, dust grains in particle accelerators tend to acquire a net charge with opposite polarity to the one of the beam: negative in the LHC and positive in electron storage rings. The resulting attractive force was historically observed in electron storage rings and just recently confirmed in the LHC [9,10]. However, the general description of the dynamics of charged dust grains in an attractive logarithmic potential like the one of a beam of particles is yet to be done. The focus of the following sections is to give a physical and mathematical framework to describe such dynamics. A similar applied case was discussed for the Orbitron of the University of Wisconsin, where electrons are injected between two concentric cylinders [51] and provides insightful results for the present paper. Grains directly attracted toward the center of the beam, as observed in the LHC (see Sec. II), are in fact a particular case of the more general solution to this problem, which is that charged grains orbit the beam. To simplify the

problem, the orbiting grains and the beam will be assumed to lie in free space, neglecting the effect of image charges on the beam screen. This approximation is valid for most transverse positions, up to a few millimeters away from the surface of the beam screen. Additionally, since the release mechanism of dust grains in the LHC is not yet understood, the grains will be assumed to conserve their original charge-to-mass ratio ($10^{-5} \text{ C/kg} \leq |Q/m| \leq 10^{-2} \text{ C/kg}$, for $5 \mu\text{m} \leq R \leq 50 \mu\text{m}$) when leaving the beam screen. The case of time-dependant charge-to-mass ratios will be discussed later, in Sec. V.

A. Logarithmic potential dynamics

The problem under study is the one of a charged body in a central potential, where the electric field comes from a beam of protons or electrons. With the range of possible charge-to-mass ratios for the grains, the expected speed is in the order of 1 m/s and the beam can be considered continuous, neglecting any bunching. For a Gaussian beam, the electric field in free space is given by the Bassetti-Erskine formula [52]. For the cylindrically symmetric case, the field can also be found from Gauss's law as follows:

$$E_r(r) = \frac{\lambda}{2\pi\epsilon_0 r} \left(1 - e^{-\frac{r^2}{2\sigma^2}}\right), \quad (16)$$

where r is the radial position from the center of the beam, λ is the linear charge density of the beam, and σ is the standard deviation of the particle distribution. For the LHC, $\lambda = N_p e/C$ with C being the LHC circumference and N_p is the number of protons in the beam. One can show that the corresponding electric potential is

$$V(r) = V_0 \left[\frac{1}{2} \text{Ei} \left(-\frac{r^2}{2\sigma^2} \right) - \ln(r/r_B) \right] \quad (17)$$

$$\approx -V_0 \ln(r/r_B) \quad \text{for } r \gg \sigma, \quad (18)$$

where $\text{Ei}(x) = -\int_{-x}^{\infty} \frac{e^{-t}}{t} dt$ is the exponential integral, r_B is the position of zero potential (generally set at the boundary) and $V_0 = \frac{\lambda}{2\pi\epsilon_0}$. When r reaches a few σ , only the logarithmic term remains in the potential and the beam can be approximated by an infinitely long charge-carrying wire. At 2σ , the error from this approximation is already below 0.5%. If stable orbits for a charged grain exist, they have to be located at $r \gg \sigma$ to avoid any interaction with the high energy particles from the beam, which directly satisfies the approximation. In the following sections, only the logarithmic approximation of the beam potential Eq. (18) will be used.

Consider a dust grain of mass m carrying a charge Q , subject to the central electric potential $V(r)$ and a potential vector \vec{A} , coming from the magnetic field of the accelerator magnets. The Hamiltonian of the system is

$$\mathcal{H} = \frac{1}{2m} |\vec{P} - Q\vec{A}|^2 + QV(r) + mgy, \quad (19)$$

where \vec{P} is the momentum and g is the gravitational constant. For small magnetic (\mathcal{H}_B) and gravitational (\mathcal{H}_g) contributions to the Hamiltonian, one can write $\mathcal{H} = \mathcal{H}_0 + \mathcal{H}_B + \mathcal{H}_g$ and treat them as a perturbation to the central Hamiltonian \mathcal{H}_0 , which is written in cylindrical coordinates (r, ϕ, z) as

$$\mathcal{H}_0 = \frac{P_r^2}{2m} + \frac{P_\phi^2}{2mr^2} + QV(r). \quad (20)$$

From the Lagrangian \mathcal{L} , one can show that $P_\phi = \partial\mathcal{L}/\partial\dot{\phi} = mr^2\dot{\phi} = L$ is the angular momentum and that $P_r = \partial\mathcal{L}/\partial\dot{r} = m\dot{r}$ is the radial momentum. In the following sections, characteristic quantities and equations relevant to the study of orbits in a logarithmic potential are derived. In a first approximation, the magnetic and gravitational contributions are neglected. In a second approximation, the effect of gravity is added to the Hamiltonian. The effect of the magnetic field is not considered in this work, due to the expected small grain velocity.

B. Case of charge-carrying wire without gravity

Neglecting the effect of the gravitational and magnetic fields as in Eq. (20), Hamilton's equations take the form:

$$\begin{aligned} \dot{r} &= \frac{P_r}{m}, & \dot{\phi} &= \frac{P_\phi}{mr^2} \\ \dot{P}_r &= \frac{P_\phi^2}{mr^3} - Q \frac{d}{dr} V(r), & \dot{P}_\phi &= 0. \end{aligned} \quad (21)$$

Due to the logarithmic potential, the equations of motion $r(t)$ and $\phi(t)$ cannot be expressed analytically [51] and the Eq. (21) is integrated numerically. Since the potential leads to a central force field, one can show that the solution for any logarithmic potential yields orbiting motion, where the orbits are always bounded, but not necessarily closed [53].

In order to reach an understanding of the resulting orbits, a conserved quantity that scales with the angular momentum of the orbiting grain as well as its charge-to-mass ratio is introduced. The orbital stiffness, \mathcal{S} , is defined as

$$\mathcal{S} \equiv \frac{h^2}{Q/m}, \quad (22)$$

where h is the specific angular momentum $h = L/m$. \mathcal{S} has units of Vm^2 . One can show that $\mathcal{S} = \frac{a_c}{a_E} V_0 r^2$, where a_c is the necessary centripetal acceleration for circular motion at a given radius and a_E is the central acceleration due to the electric field. Hence, \mathcal{S} describes the balance between the centripetal and electric forces. Over the course of an orbital period, the different contributions oscillate, but \mathcal{S} remains

constant. With this definition, the central Hamiltonian in the logarithmic approximation of the beam can be written as

$$\begin{aligned} \mathcal{H}_0 &= \frac{P_r^2}{2m} + Q \left[\frac{\mathcal{S}}{2r^2} - V_0 \ln(r/r_B) \right] \\ &= \frac{P_r^2}{2m} + Q\tilde{V}_0(r), \end{aligned} \quad (23)$$

where $\tilde{V}_0(r)$ is the effective potential of \mathcal{H}_0 , which is the sum of the angular kinetic energy and the potential energy. For a given total energy E , the point of closest approach r_{\min} and the point of furthest approach r_{\max} from the origin can be found by setting the radial momentum $P_r = 0$ since they correspond to turning points. These extrema are, therefore, the roots of the following expression:

$$\frac{E}{Q} - \frac{\mathcal{S}}{2r^2} + V_0 \ln(r/r_B) = 0, \quad (24)$$

which leads to $r_{\min} = \sqrt{\frac{\mathcal{S}/V_0}{W_{-1}(\xi)}}$ and $r_{\max} = \sqrt{\frac{\mathcal{S}/V_0}{W_0(\xi)}}$ where W_n is the n th branch of the Lambert W function and $\xi = \frac{\mathcal{S}}{V_0 r_B^2} \exp(\frac{2E}{QV_0})$. For a given orbital stiffness, there is precise energy for which $r_{\min} = r_{\max} = r_c$, in which case the orbit is circular. This energy corresponds to the extremum of the effective potential and is found at

$$r_c = \sqrt{-\mathcal{S}/V_0} \quad (25)$$

which is real when \mathcal{S} and λ are of opposing signs. In the LHC, \mathcal{S} is negative due to the negative charge carried by dust grains and λ is positive. Figure 6 shows the effective potential for different orbital stiffnesses as a function of the radial position

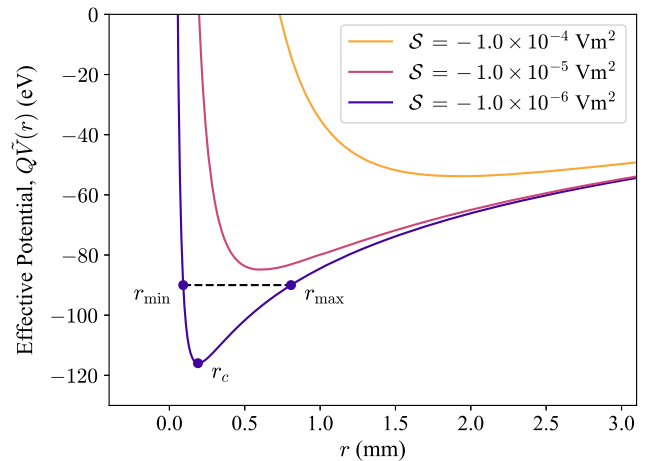


FIG. 6. Effective potential as a function of r with $N_p = 2.5 \times 10^{14} \text{ p}^+$, $Q = -1e$, and $r_B = 23.25 \text{ mm}$. r_B is set to be the horizontal distance between the beam and the beam screen. r_c is shown for a given \mathcal{S} and r_{\min} , r_{\max} are shown for a given E .

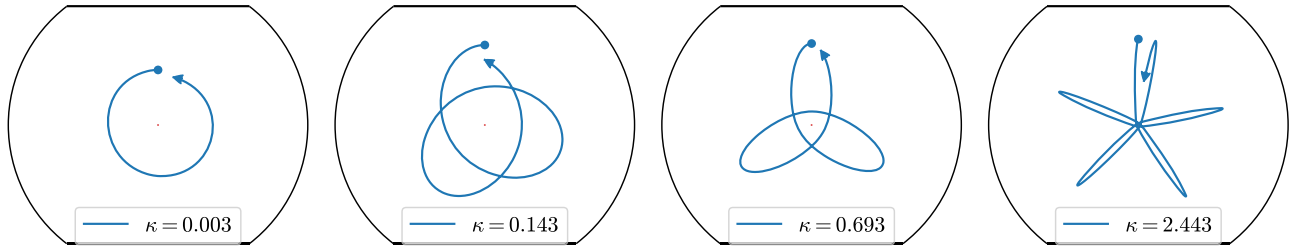


FIG. 7. Example of orbits in the logarithmic potential of the LHC beam for distinct shape parameters. As $\kappa \rightarrow 0$, the orbit becomes circular and for $\kappa \rightarrow \infty$, the orbit degenerates into a straight line going through the beam. \mathcal{S} makes the orbit scale radially but does not change the shape. The beam screen has a width of 46.5 mm and a height of 36.9 mm.

for the case of the LHC. From the solutions of Eq. (24), one can show that an orbital stiffness between -3×10^{-6} and -10^{-4} Vm^2 allows r_{\min} to lie inside the LHC beam (between 1σ and 6σ , with an rms beam size of $\sigma = 150 \mu\text{m}$) for any grain while r_{\max} remains smaller than the distance to the beam screen. Experimentally, these are the stiffness values that can lead to measurable beam losses following beam-dust interactions. For stiffnesses above 10^{-4} Vm^2 in amplitude, r_{\min} is always outside of the beam.

For the particular case of a circular orbit with energy E_c , the angular kinetic energy depends only on the charge of the dust grain, $K_{\phi,c} = E_c + QV_0 \ln(r_c/r_B) = -\frac{1}{2}QV_0$. This allows for the definition of a dimensionless *shape parameter*, $\kappa(E, \mathcal{S})$, which quantifies the deviation of a given orbit from the circular one:

$$\kappa \equiv \frac{E - E_c}{2K_{\phi,c}} = -\frac{E}{QV_0} - \frac{1}{2} \left[1 + \ln \left(\frac{-\mathcal{S}}{V_0 r_B^2} \right) \right]. \quad (26)$$

κ is similar to the orbit eccentricity in planetary motion. Since the circular orbit energy is, by definition, the minimal energy allowed for a given \mathcal{S} , κ is positive and increases with the difference in energy from the circular orbit. Based on the work from Hooverman [51], one can show that κ uniquely defines the shape of the orbit. For $\kappa = 0$, the orbit is circular, and for $\kappa \rightarrow \infty$, the orbit degenerates into a straight line going through the center of the beam. After $\kappa \approx 2.5$, the orbit is already significantly elongated and approaches the beam screen up to a few mm for the range of orbital stiffnesses mentioned previously. Figure 7 shows examples of orbits in the logarithmic potential of the LHC beam for different shape parameters. The effect of varying the stiffness is to scale the orbits radially, but the shape is preserved for equal κ .

1. Period of radial oscillation

Because of the cylindrical symmetry, the angular position ϕ is of little interest for this problem. On the other hand, the evolution of the radial position is critical as beam-dust interactions cause beam losses to arise for small radial positions and because orbiting grains are stopped by the chamber's walls for large radial positions. As shown in

Fig. 7, the position oscillates between r_{\min} and r_{\max} over the course of an orbit. The period of radial oscillation, T_r , can be obtained from the Hamiltonian following:

$$T_r = \sqrt{2m} \int_{r_{\min}}^{r_{\max}} \frac{dr}{\sqrt{E - Q\tilde{V}_0(r)}}. \quad (27)$$

Except for the limit cases of $\kappa \rightarrow 0$ and $\kappa \rightarrow \infty$, this integral cannot be solved analytically and must be evaluated numerically [51]. The general result with the two limit cases can be written in the compact form:

$$T_r = \tau e^{-E/(QV_0)} f(\kappa) \quad \text{with} \quad \begin{aligned} f(\kappa \rightarrow 0) &= \frac{1}{\sqrt{e}} \\ f(\kappa \rightarrow \infty) &= \frac{1}{\sqrt{\pi}}, \end{aligned} \quad (28)$$

where $\tau = 2\pi \sqrt{\frac{m}{-2QV_0}} r_B$ and $f(\kappa)$ is a dimensionless function of κ only. Based on the numerical integration of Eq. (27) shown in Fig. 8, one can see that $f(\kappa)$ decreases monotonically as κ increases and asymptotically reaches its limit of $1/\sqrt{\pi}$. To allow for efficient analytic calculations, the following approximation for $f(\kappa)$ is proposed:

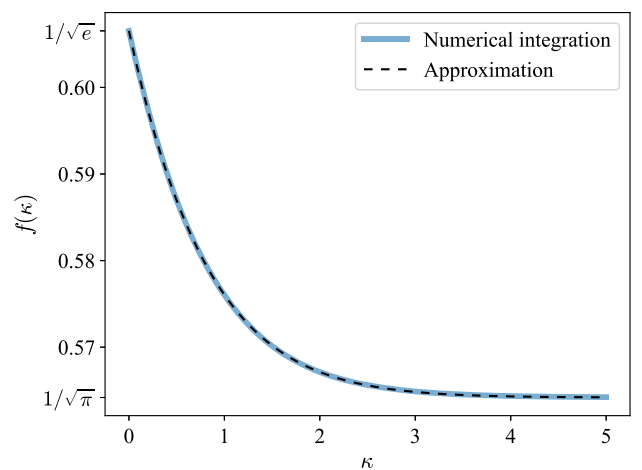


FIG. 8. Comparison of the dimensionless function $f(\kappa)$ obtained from numerical integration and from the approximation Eq. (29). The error from the approximation is below 0.014% for any κ .

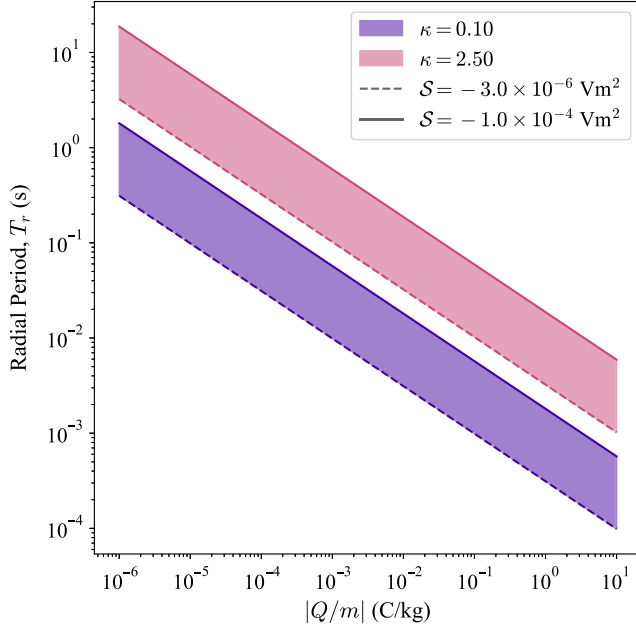


FIG. 9. Period of the radial oscillation for dust grains orbiting the LHC beam as a function of the charge-to-mass ratio. The period is smaller for quasicircular orbits ($\kappa = 0.1$) than for elongated orbits ($\kappa = 2.5$) but also scales with \mathcal{S} .

$$f(\kappa) \approx \left(\frac{1}{\sqrt{e}} - \frac{1}{\sqrt{\pi}} \right) e^{A\kappa(B-\kappa)} + \frac{1}{\sqrt{\pi}}, \quad (29)$$

where $A = 6.1125 \times 10^{-2}$ and $B = -19.8135$ are two dimensionless fitting parameters. The error from this approximation is below 0.014% for any κ .

The radial period evaluated from Eq. (28) can span several orders of magnitude as it varies with \mathcal{S} , κ , and Q/m . Choosing once again the stiffness such that $r_{\min} < 6\sigma$ and $r_{\max} < r_B$, one finds the oscillation periods shown in Fig. 9. If $|\mathcal{S}| > 10^{-4} \text{ Vm}^2$, the grain never interacts with the beam. In that case, the radial period is longer than 1 ms for high $|Q/m| \sim 10^1 \text{ C/kg}$ and longer than 2 s for small $|Q/m| \sim 10^{-6} \text{ C/kg}$. For stiffnesses smaller in amplitude, beam-dust interactions can take place and the radial period can be as small as 10^{-4} s , assuming that the orbit is not affected by the interaction with the beam. With the range of charge-to-mass ratios found in previous sections, the expected period lies between 3 and 100 ms. However, as will be discussed in Sec. V, the charge-to-mass ratio is not constant when the grain interacts with the beam, which can significantly alter the orbit of the grain.

C. Charge-carrying wire with gravity

The previous results were derived assuming that the effect of gravity could be neglected, which is the case for large charge-to-mass ratios. Adding the contribution of gravity to the Hamiltonian, the effective potential becomes

$$\tilde{V}_g(r, \phi) = \frac{\mathcal{S}(r, \phi)}{2r^2} - V_0 \ln(r/r_B) + \frac{1}{Q/m} g r \sin(\phi), \quad (30)$$

where the grain stiffness $\mathcal{S}(r, \phi)$ is no longer constant, along with the angular momentum, because of the ϕ dependence of the potential. Taking the Taylor expansion around r_c for the last two terms of the potential, regrouped as $U_g = -V_0 \ln(r/r_B) + \frac{1}{Q/m} g r \sin(\phi)$, one finds

$$\begin{aligned} U_g(r) &= U_g(r_c) + \left[-\frac{V_0}{r_c} + \frac{1}{Q/m} g \sin(\phi) \right] (r - r_c) + \dots \\ &= U_0(r_c) + \left[-\frac{V_0}{r_c} + \frac{1}{Q/m} g \sin(\phi) \right] r + \frac{V_0}{r_c} r_c + \dots \\ &\approx U_0(r) \quad \text{for } r \rightarrow r_c \quad \text{if } \frac{g}{|Q/m|} \ll \frac{|V_0|}{r_c}, \end{aligned} \quad (31)$$

where $U_0(r) = -V_0 \ln(r/r_B)$ is the last term of the original effective potential. The result Eq. (31) gives the formal condition under which gravity can be neglected, in which case the stiffness is once again constant. As an example, for the stiffness values shown in Fig. 9, $|V_0|/r_c$ is an order of magnitude higher than $g/(|Q/m|)$ when $|Q/m| > 10^{-3} \text{ C/kg}$ and gravity can be neglected.

For a small but non-negligible gravitational contribution, the orbits are shifted vertically downwards. One can show that there is no inertial reference frame in which the angular momentum of the grain is conserved since the angular velocity is always higher in the lower half of the orbit compared with the upper half. However, there is a reference frame in which the variations of the angular momentum are minimized. Consider a primed reference frame (r', ϕ') , shifted downwards by a distance d such that $y' = y + d$. The radial position in that frame is $r'^2 = r^2/(1 + \epsilon')$, with $\epsilon' = (\frac{d}{r})^2 - 2(\frac{d}{r}) \sin(\phi')$, and the effective potential becomes

$$\begin{aligned} \tilde{V}_g(r', \phi') &= \frac{\mathcal{S}_{\text{eff}}}{2r'^2} - \frac{V_0}{2} \ln(r'^2(1 + \epsilon')/r_B) \\ &\quad + \frac{1}{Q/m} g(r' \sin(\phi') - d), \end{aligned} \quad (32)$$

where $\mathcal{S}_{\text{eff}} = \frac{\mathcal{S}(r, \phi)}{1 + \epsilon'}$. Assuming that $d \ll r'$, the approximation $\ln(1 + \epsilon') \approx \epsilon'$ can be used to get

$$\tilde{V}_g(r', \phi') \approx \tilde{V}_0(r') \Big|_{\mathcal{S}=\mathcal{S}_{\text{eff}}} - \frac{V_0}{2} \epsilon' + \frac{1}{Q/m} g(r' \sin(\phi') - d). \quad (33)$$

Neglecting second order terms in d/r' and assuming that r' remains close to $r'_c = \sqrt{-\mathcal{S}_{\text{eff}}/V_0}$, one finds that the two ϕ' dependent terms in Eq. (33) cancel out when

$$d = -r'_c \left[\frac{\sin(\phi')}{\frac{V_0(Q/m)}{gr'_c} \sin(\phi') - 1} \right] \approx -\frac{g}{V_0(Q/m)} r'_c{}^2, \quad (34)$$

where the last result is the averaged value over a full ϕ' period. In this shifted frame, the effective potential takes the form of the original potential with a stiffness \mathcal{S}_{eff} . The center of the orbit is found below the beam, shifted by an amount Δy_g :

$$\Delta y_g \approx \left[\left(\frac{d}{r_c} \right)^2 - 2 \left(\frac{d}{r_c} \right) \right] r_c - d \approx -3d. \quad (35)$$

V. EFFECT OF BEAM-DUST INTERACTIONS

In the previous sections, the charge of the orbiting dust grain was assumed to be constant in time for simplicity. However, this is not the case for dynamic conditions where the grain moves in the transverse plane, since it will be subject to varying electron cloud densities and varying synchrotron radiation distributions. Moreover, for orbits with $r_{\text{min}} < 6\sigma$, every passage close to the center of the beam leads to beam-dust interactions, which creates beam losses and significantly alters the charge of the dust grain. As discussed in previous work [9], the energy deposited by the beam in the dust grain releases knock-on electrons and contributes to an additional positive charging current. Hence, close to the center of the beam, the net charging current is expected to be positive, both in the LHC and in negative-particle accelerators. Under these time-varying conditions, the motion of the grain can be described by a succession of orbits with instantaneous parameters $Q(t)$, $E(t)$, $\mathcal{S}(t)$, and $\kappa(t)$.

To illustrate this effect, a simulation tool developed at CERN [9] was used. The grain dynamics is computed by numerically solving Hamilton's equation (21). As the grain interacts with the LHC beam, the charging current due to the energy deposited by the protons is computed, as well as the beam losses produced from the inelastic collisions with the nuclei of the dust grain. Figure 10 shows an example of the orbital motion for such a case as well as the resulting beam losses. In this example, for every passage close to the beam center, the grain is subject to a positive charging current but remains negatively charged. As a result, $\kappa(t)$ increases and the orbit becomes more elongated. Since $|Q(t)/m|$ decreases, $|\mathcal{S}(t)|$ increases and so does the instantaneous value of r_c . When the grain leaves the vicinity of the beam, the gravitational force dominates over the attractive force and the grain is sent to the beam screen.

As long as the grain remains negatively charged, the orbit is bounded and the instantaneous orbit parameters are tied together, as seen in Eqs. (22) and (26). Figure 11 shows the evolution of $\kappa(t)$, $|Q(t)|$, and $|\mathcal{S}(t)|$ during one close approach to the beam. Assuming that r_{max} lies outside of the beam, the grain is only ionized when $r \rightarrow r_{\text{min}}$ and the orbit parameters evolve in a step-wise manner. If the grain

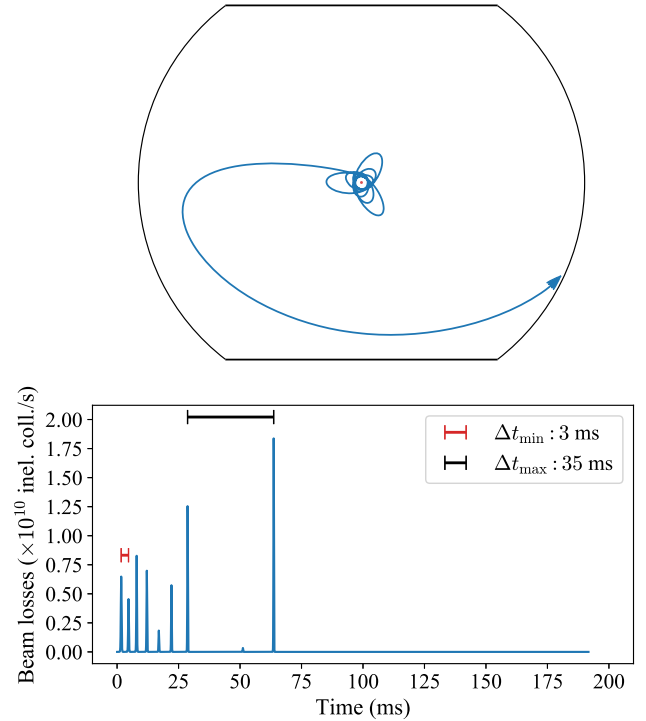


FIG. 10. Example trajectory for a negatively charged dust grain orbiting the LHC beam. With every passage close to the beam, the grain is subject to a positive charging current, and the instantaneous shape parameter increases. The grain radius is $50 \mu\text{m}$ and the initial stiffness is $\mathcal{S} = -1.18 \times 10^{-5} \text{Vm}^2$. The simulated inelastic collision rate from the beam-dust interactions is also shown, with peaks in the order of 10^{10} inelastic collisions per second, separated by a few ms.

is too close to the center of the beam, the charging rate is such that the orbit rapidly grows and the grain is sent to the beam screen. On the other hand, if the grain is far from the beam, the charging rate is small and the orbit can last for

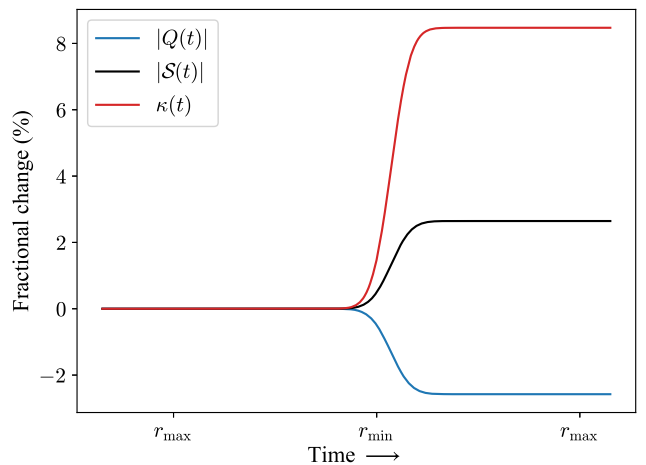


FIG. 11. Example of the evolution of the instantaneous orbit parameters in the LHC during one close approach to the beam. The grain is subject to a positive charging current, but the net charge remains negative.

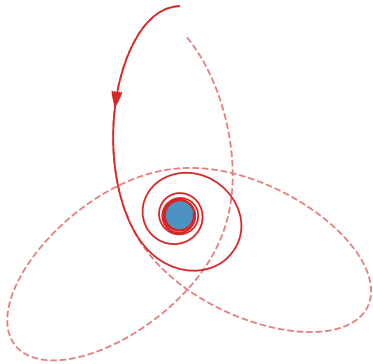


FIG. 12. Example of the orbital motion of a positively charged dust grain being further ionized and trapped in a negative-particle beam. The dashed line shows the corresponding orbit for a constant charge if no beam-dust interactions were taking place.

several seconds, with small beam losses. In the example of Fig. 10, the radial position is $r_{\min} \sim 4.7\sigma$, which leads to a collision rate in the order of 10^{10} inelastic collisions per second and the grain is sent to the beam screen after 190 ms.

The approach developed for the case of the LHC can be extended to the case of a negative-particle accelerator. For a positively charged grain orbiting and interacting with a negative-particle beam, the result is the opposite: the positive charge of the grain increases, the grain spirals inward toward the center of the beam and it remains trapped. As the positive charge of the grain increases, both the shape parameter and the stiffness decrease in amplitude. The orbit evolves toward a circular one and $r_c \propto \sqrt{S}$ decreases continuously. An example of such orbital motion is shown in Fig. 12.

A. Multipeak measurement in the LHC

While the majority of beam loss events caused by dust grains in the LHC show a single Gaussian-like signal, a significant portion of them has more than one peak. For LHC Run II data, about 30% of the recorded events show more than one peak, sometimes overlapping each other with 100 μs separation, sometimes separated by several ms. Figure 13 shows three examples of multipeak events measured in the LHC where the peak separation is between 4 and 112 ms and Fig. 14 shows two examples of overlapping peaks, where the peak separation is below 2 ms. This observation has been discussed in the past [11] but is not yet understood.

Based on the results of this paper, the hypothesis of having dust grains orbiting the LHC beam is proposed to explain the multipeak events observed experimentally. The peak separations found in the measurements of Fig. 13 are between 4 and 112 ms, which corresponds to the radial period of oscillation for orbiting grains of $10^{-5} \text{ C/kg} \leq |Q/m| \leq 10^{-2} \text{ C/kg}$ according to Fig. 9. Moreover, the amplitude of the losses, which depends on the grain size, the grain composition, and the distance from the beam, is

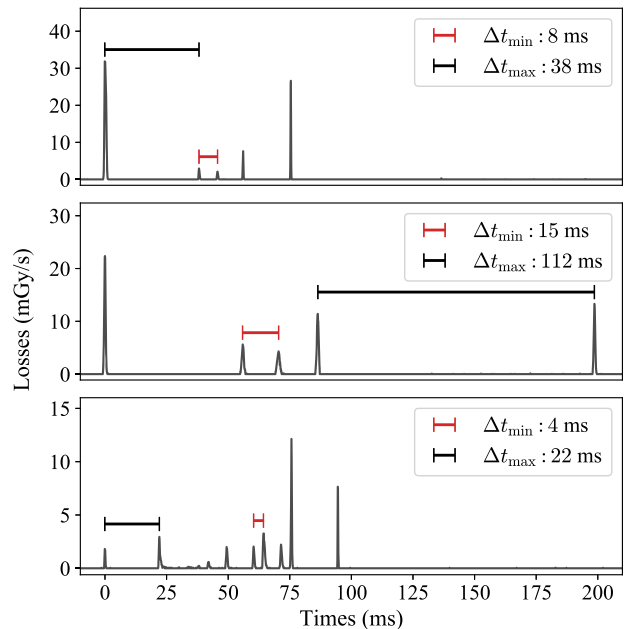


FIG. 13. Measurement of multipeaks beam loss events attributed to dust grains during LHC Run II (2015–2018). Given the response factor of the beam loss monitors, the amplitude of the losses is in the order of 10^9 – 10^{10} inelastic collisions/s. For each event, the shortest and longest peak separation is identified.

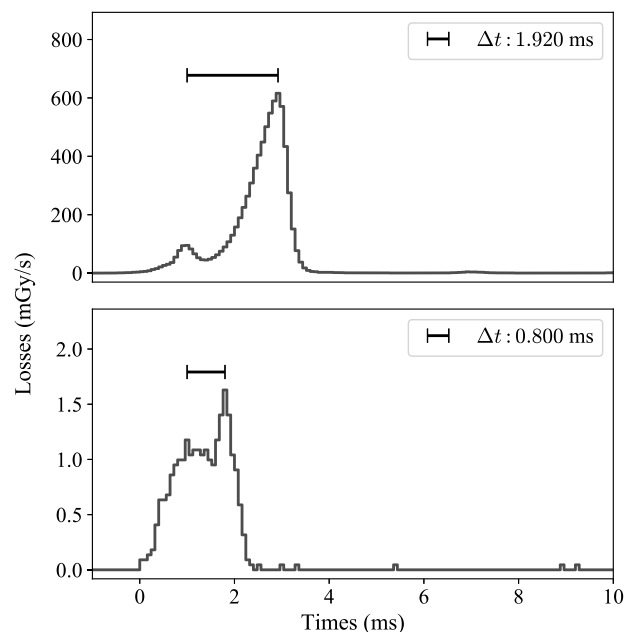


FIG. 14. Measurement of beam loss events with overlapping multipeaks attributed to dust grains during LHC Run II. Given the response factor of the beam loss monitors, the amplitude of the losses is in the order of 10^9 – 10^{11} inelastic collisions/s.

consistent with the numerical example given in Fig. 10. Indeed, the response factor of the LHC beam loss monitors is in the order of 10^{-12} Gy/inelastic collisions, which leads to losses in the order of 10^9 – 10^{10} inelastic collisions/s for the multipeak measurement presented in Fig. 13. For the shorter peak separation found in Fig. 14, a charge-to-mass ratio of 10^{-1} C/kg is required, which is consistent with previous studies [10] and with the results presented in this paper for dust grains smaller than $5\ \mu\text{m}$ or density ratios larger than 10^7 (see Table II).

From these observations, one can conclude that there is a set of instantaneous orbit parameters for which the expected orbital period and the amplitude of the beam losses are consistent with the measurements presented. However, since the release mechanism of dust grains in the LHC is still to be understood, the study of the initial conditions required to place a dust grain in such orbit is left for future work. Because of the rapid charging of the grain during the interaction with the beam, the instantaneous orbit parameters change significantly between successive orbital periods. As a result, the global dynamics under these time-varying conditions is chaotic and highly sensitive to the choice of initial conditions for the dust grain.

Alternative explanations for multipeak events in the LHC should also be considered, in particular, the possibility of having independent dust grains interacting with the beam within a short time window. However, because of the time scale involved (ms) and the general rate of observation of these events (few occurrences per hour), the plausibility of this hypothesis depends on the release mechanism of dust grains. If the release mechanism follows a stochastic process, the probability of observing two independent grains on the same beam loss monitor of the LHC within a few ms is extremely low. On the other hand, if the release of dust grains is caused by some perturbation of the environment around the beam screen (mechanical vibration, electromagnetic kick, etc.), this alternative hypothesis is plausible. Finally, for overlapping multipeak events separated by a few $100\ \mu\text{s}$, the possibility of having nonspherical dust grain (e.g., needle shape), interacting sequentially with the beam due to an induced rotation or due to the irregular shape of the grain, has to be considered.

VI. CONCLUSION

This paper presents the charging mechanisms for dust grains in particle accelerators and the resulting dynamics in a logarithmic potential. Principles from dusty plasma physics were applied to the environment of particle accelerators, where electron clouds and synchrotron radiation contribute to the charging of isolated dust grains. It was found that the balance of the electron collection current, the secondary electron current, and the photoelectric current determines the equilibrium surface potential of spherical dust grains. The equations presented in this paper provide an explanation for the recent observation of negatively

charged grains in the LHC and for the historical observation of positively charged grains in electron storage rings.

For electron clouds dominated by low energy electrons, the ratio of the electron density to the photon density is found to be a critical parameter for the polarity acquired by charged grains. For high electron cloud densities like in the LHC, the electron collection current overcomes the photoelectric emission current and grains acquire a net negative charge. The expected equilibrium surface potential is found to be in the order of -10 to -100 V, which corresponds to charge-to-mass ratios between 10^{-5} C/kg $\leq |Q/m| \leq 10^{-2}$ C/kg for radii between $5\ \mu\text{m} \leq R \leq 50\ \mu\text{m}$. In electron storage rings, the photoelectric emission current dominates, which leads to positively charged grains. Otherwise, for grains mainly bombarded by electrons of a few hundred eV, for which the secondary electron yield is above unity, the net charge acquired is positive under all conditions.

Since dust grains tend to acquire a net charge with opposite polarity to one of the beams, the dynamics of orbiting dust grains in the logarithmic potential of a beam of particles was discussed. It was shown that gravity can be neglected for sufficient charge-to-mass ratio or small enough radial positions. The orbital stiffness and the shape parameter were introduced to describe the resulting orbits. An analytic expression for the radial period of oscillation was also presented. Together, these quantities allow for a complete description of the orbits and link the charge-to-mass ratio of an orbiting dust grain to the amplitude and temporal separation of beam losses resulting from beam-dust interactions. Experimental measurements of beam losses with multiple peaks separated by a few hundred ms were presented. The hypothesis of having dust grains with charge-to-mass ratios between 10^{-5} C/kg $\leq |Q/m| \leq 10^{-1}$ C/kg was suggested to explain the peak separation and the amplitude from these measurements.

This paper presents new ways of explaining historical observations of dust grain events in particle accelerators, based on concepts from plasma physics. In the case of the LHC, some open questions remain, in particular, concerning the release mechanism of the grains. Is the release triggered by mechanical vibrations, electrostatic levitation, or straightforward attraction from the beam? To validate the completeness of the theory presented in this paper, a dedicated set of experimental investigations is required. Suitable experiments should be based on the results of this paper as well as on the extensive work that has been carried out over two decades in plasma physics and on the surface formation of airless planetary bodies. Experiments in the LHC and other high intensity beam facilities will be critical to understand and mitigate the impact of dust grains on the operation of future accelerators.

ACKNOWLEDGMENTS

This work was supported by the High Luminosity Large Hadron Collider project.

- [1] H. Saeki, T. Momose, and H. Ishimaru, Observations of dust trapping phenomena in the TRISTAN accumulation ring, and a study of dust removal in a beam chamber, *Rev. Sci. Instrum.* **62**, 874 (1991).
- [2] D. Sagan, Mass and charge measurement of trapped dust in the CESR storage ring, *Nucl. Instrum. Methods Phys. Res. Sect. A* **330**, 371 (1993).
- [3] F. Zimmermann, Trapped dust in HERA and DORIS, DESY, DESY-HERA-93-08, 1993, <https://cds.cern.ch/record/252789>.
- [4] S. Terui, Y. Suetsugu, T. Ishibashiq, M. Shirai, K. Shibata, K. Kanazawa, and H. Hisamatsu, Observation of pressure bursts in the SuperKEKB positron ring, in *Proceedings of 9th International Particle Accelerator Conference, IPAC-2018, Vancouver, BC, Canada* (JACoW, Geneva, Switzerland, 2018), [10.18429/JACoW-IPAC2018-WEPML058](https://doi.org/10.18429/JACoW-IPAC2018-WEPML058).
- [5] G. Papotti, M. Albert, B. Auchmann, E. B. Holzer, M. Kalliokoski, and A. Lechner, Macroparticle-induced losses during 6.5 TeV LHC operation, in *Proceedings of 7th International Particle Accelerator Conference, IPAC-2016, Busan, Korea*, International Particle Accelerator Conference (JACoW, Geneva, Switzerland, 2016), pp. 1481–1484, [10.18429/JACoW-IPAC2016-TUPMW023](https://doi.org/10.18429/JACoW-IPAC2016-TUPMW023).
- [6] T. Baer, M. J. Barnes, F. Cerutti, A. Ferrari, N. Garrel, B. Goddard, E. B. Holzer, S. Jackson, A. Lechner, V. Mertens, M. Misiowiec, E. Nebot Del Busto, A. Nordt, J. Uythoven, V. Vlachoudis, J. Wenninger, C. Zamantzas, F. Zimmermann, and N. F. Martinez, UFOs in the LHC: Observations, studies and extrapolations, in *Proceedings of the 3rd International Particle Accelerator Conference, New Orleans, LA, 2012* (IEEE, Piscataway, NJ, 2012).
- [7] B. Goddard, P. Adraktas, T. Baer, M. J. Barnes, F. Cerutti, A. Ferrari, N. Garrel, A. Gerardin, M. Guinchard, A. Lechner, A. Masi, V. Mertens, R. Morón Ballester, S. Redaelli, J. Uythoven, V. Vlachoudis, and F. Zimmermann, Transient beam losses in the LHC injection kickers from micron scale dust particles, in *Proceedings of the 3rd International Particle Accelerator Conference, New Orleans, LA, 2012* (IEEE, Piscataway, NJ, 2012).
- [8] B. Auchmann, J. Ghini, L. Grob, G. Ladarola, A. Lechner, and G. Papotti, How to survive a UFO attack, in *Proceedings of the 6th Evian Workshop on LHC Beam Operation, Evian Les Bains, France, 2015* (CERN, Geneva, 2016).
- [9] B. Lindstrom, P. Bélanger, A. Gorzawski, J. Kral, A. Lechner, B. Salvachua, R. Schmidt, A. Siemko, M. Vaananen, D. Valuch, C. Wiesner, D. Wollmann, and C. Zamantzas, Dynamics of the interaction of dust particles with the LHC beam, *Phys. Rev. Accel. Beams* **23**, 124501 (2020).
- [10] A. Lechner, P. Bélanger, I. Efthymiopoulos, L. Grob, B. Lindstrom, R. Schmidt, and D. Wollmann, Dust-induced beam losses in the cryogenic arcs of the CERN Large Hadron Collider *Phys. Rev. Accel. Beams* **25**, 041001 (2022).
- [11] N. F. Martinez, F. Zimmermann, T. Baer, M. Giovannozzi, E. B. Holzer, E. Nebot, A. Nordt, M. Sapinski, and Z. Yang, Simulation studies of macroparticles falling into the LHC proton beam, in *Proceedings of the 2nd International Particle Accelerator Conference, San Sebastián, Spain, 2011*, International Particle Accelerator Conference (JACoW, Geneva, 2011), pp. 634–636, <https://accelconf.web.cern.ch/ipac2011/papers/mops017.pdf>.
- [12] B. Lindstrom, A. Apollonio, P. Bélanger, M. Dziadosz, A. Gorzawski, L. Grob, E. B. Holzer, A. Lechner, R. Schmidt, M. Valette, D. Valuch, and D. Wollmann, Results of UFO dynamics studies with beam in the LHC, in *Proceedings of 9th International Particle Accelerator Conference, IPAC-2018, Vancouver, BC, Canada* (JACoW, Geneva, Switzerland, 2018).
- [13] S. Rowan, A. Apollonio, B. Auchmann, A. Lechner, O. Picha, W. Riegler, H. Schindler, R. Schmidt, and F. Zimmermann, Interactions between macroparticles and high-energy proton beams, in *Proceedings of 6th International Particle Accelerator Conference, IPAC-2015, Richmond, VA* (JACoW, Geneva, Switzerland, 2015), p. 2112.
- [14] A. Lechner *et al.*, BLM thresholds and UFOs, *Proceedings of the 7th Evian Workshop on LHC Beam Operation, Evian Les Bains, France, 2016* (CERN, Geneva, 2016).
- [15] A. Lechner, B. Auchmann, T. Baer, C. Bahamonde Castro, R. Bruce, F. Cerutti, L. S. Esposito, A. Ferrari, J. M. Jowett, A. Mereghetti, F. Pietropaolo, S. Redaelli, B. Salvachua, M. Sapinski, M. Schaumann, N. V. Shetty, and V. Vlachoudis, Validation of energy deposition simulations for proton and heavy ion losses in the CERN Large Hadron Collider, *Phys. Rev. Accel. Beams* **22**, 071003 (2019).
- [16] L. K. Grob, C. Neves, A. Apollonio, J. Descarraga Busom, C. Charvet, A. T. Perez Fontenla, E. Garcia-Tabares Valdivieso, H. Kos, and R. Schmidt, Dust analysis from LHC vacuum system to identify the source of macro particle-beam-interactions, in *Proceedings of 10th International Particle Accelerator Conference, IPAC-2019, Melbourne, Australia, 2019* (JACoW, Geneva, Switzerland, 2019), p. 1082.
- [17] J. Rennilson and D. Criswell, Surveyor observations of lunar horizon-glow, *The Moon* **10**, 121 (1974).
- [18] X. Wang, J. Schwan, H. W. Hsu, E. Grün, and M. Horányi, Dust charging and transport on airless planetary bodies, *Geophys. Res. Lett.* **43**, 6103 (2016).
- [19] J. Schwan, X. Wang, H. W. Hsu, E. Grün, and M. Horányi, The charge state of electrostatically transported dust on regolith surfaces, *Geophys. Res. Lett.* **44**, 3059 (2017).
- [20] M. M. Abbas, D. Tankosic, A. C. Leclair, and J. F. Spann, Charging of dust grains in astrophysical environments by secondary electron emissions, *Astrophys. J.* **756**, 41 (2012).
- [21] D. A. Mendis, Progress in the study of dusty plasmas, *Plasma Sources Sci. Technol.* **11**, A219 (2002).
- [22] A. Piel and A. Melzer, Dusty plasmas—The state of understanding from an experimentalist’s view, *Adv. Space Res.* **29**, 1255 (2002).
- [23] E. Whipple, Potentials of surfaces in space, *Rep. Prog. Phys.* **44**, 1197 (1981).
- [24] A. A. Sickafoose, J. E. Colwell, M. Horányi, and S. Robertson, Photoelectric Charging of Dust Particles in Vacuum, *Phys. Rev. Lett.* **84**, 6034 (2000).
- [25] A. A. Sickafoose, J. E. Colwell, M. Horányi, and S. Robertson, Experimental investigations on photoelectric and triboelectric charging of dust, *J. Geophys. Res.* **106**, 8343 (2001).

- [26] V. W. Chow, D. A. Mendis, and M. Rosenberg, Role of grain size and particle velocity distribution in secondary electron emission in space plasmas, *J. Geophys. Res.* **98**, 19065 (1993).
- [27] Y. Wu, G. S. Castle, I. I. Inculet, S. Petigny, and G. S. Sweig, The effect of electric field strength on the induction charge of freely levitating particles, *IEEE Trans. Ind. Appl.* **40**, 1498 (2004).
- [28] L. Musinski, T. Liu, B. Gilchrist, and A. Gallimore, Electrostatic charging of micro- and nano-particles for use with highly energetic applications, *J. Electrostat.* **67**, 54 (2009).
- [29] S. Terui, T. Ishibashi, M. Shirai, Y. Suetsugu, and K. Shibata, Report on collimator damage event in Super-KEKB, in *Proceedings of the 12th International Particle Accelerator Conference, Campinas, Brazil, 2021* (JACoW, Geneva, Switzerland, 2021).
- [30] O. Grobner, Beam induced multipacting, in *Proceedings of the Particle Accelerator Conference, Vancouver, BC, Canada, 1997* (IEEE, New York, 1997).
- [31] G. Rumolo and G. Iadarola, Electron clouds, in *Proceedings of the CAS-CERN Accelerator School* (2017), Vol. 3.
- [32] F. Zimmermann, Electron-cloud effects in the LHC, in *Mini Workshop on Electron Cloud Simulations for Proton and Positron Beams*, CERN Yellow Reports: Conference Proceedings (CERN, Geneva, 2002), [10.5170/CERN-2002-001.47](https://cds.cern.ch/record/2002-001.47).
- [33] F. Zimmermann, Electron-cloud simulations for SPS, and LHC, in *Proceedings of the 10th Workshop on LEP-SPS Performance, Chamonix, France, 2000* (CERN, Geneva, 2000), pp. 136–149, <https://cds.cern.ch/record/485871>.
- [34] G. Skripka and G. Iadarola, Beam-induced heat loads on the beam screens of HL-LHC arcs, 2019, <https://cds.cern.ch/record/2692753>.
- [35] H. Seiler, Secondary electron emission in the scanning electron microscope, *J. Appl. Phys.* **54**, R1 (1983).
- [36] R. Cimino, I. R. Collins, M. A. Furman, M. Pivi, F. Ruggiero, G. Rumolo, and F. Zimmermann, Can Low-Energy Electrons Affect High-Energy Physics Accelerators?, *Phys. Rev. Lett.* **93**, 014801 (2004).
- [37] G. Iadarola *et al.*, Beam-induced heat loads on the LHC arc beam screens with different beam and machine configurations: Experiments and comparison against simulations, Report No. CERN-ACC-NOTE-2019-0057, 2019.
- [38] N. Meyer-Vernet, Flip-flop of electric potential of dust grains in space, *Astron. Astrophys.* **105**, 98 (1982), <https://ui.adsabs.harvard.edu/abs/1982A&A...105...98M>.
- [39] A. Hofmann, Characteristics of synchrotron radiation, CERN Accelerator School Report No. CERN 98-04, 1998, [10.5170/CERN-1998-004.1](https://cds.cern.ch/record/1998-004.1).
- [40] G. Guillermo, G. Maury Cuna, and F. Zimmermann, Electron cloud build up for LHC ‘Sawtooth’ vacuum chamber, in *Proceedings of 9th International Particle Accelerator Conference, IPAC-2018, Vancouver, BC, Canada* (JACoW, Geneva, Switzerland, 2018).
- [41] V. Baglin, G. Bregliozzi, J. M. Jimenez, and G. Lanza, Synchrotron radiation in the LHC vacuum system, in *Proceedings of the 2nd International Particle Accelerator Conference, San Sebastián, Spain* (JACoW, Geneva, 2011), pp. 1563–1565.
- [42] J. C. Weingartner and B. T. Draine, Photoelectric emission from interstellar dust: Grain charging and gas heating, *Astrophys. J. Suppl. Ser.* **134**, 263 (2001).
- [43] P. K. Shukla and A. A. Mamun, *Introduction to Dusty Plasma Physics*, Series in Plasma Physics (Taylor & Francis Group, 2002), p. 281, ISBN 9781420034103.
- [44] Y. Tanimoto, T. Honda, and S. Sakanaka, Experimental demonstration and visual observation of dust trapping in an electron storage ring, *Phys. Rev. ST Accel. Beams* **12**, 110702 (2009).
- [45] F. Pedersen, Effects of highly charged solid macroparticles captured in negatively charged circulating beams, in *Proceedings of the 1987 IEEE Particle Accelerator Conference IEEE Particle Accelerator Conference* (JACoW Publishing, 1987), p. 1246, https://accelconf.web.cern.ch/p87/PDF/PAC1987_1246.PDF
- [46] H. Saeki, T. Momose, and H. Ishimaru, Experiments to trap dust particles by a wire simulating an electron beam, *Rev. Sci. Instrum.* **62**, 2568 (1991).
- [47] H. Saeki, T. Momose, and H. Ishimaru, Motions of trapped dust particles around the electron beam in the TRISTAN accumulation ring, *Rev. Sci. Instrum.* **62**, 2558 (1991).
- [48] C. M. Celata, Electron cloud dynamics in the Cornell Electron Storage Ring Test Accelerator wiggler, *Phys. Rev. ST Accel. Beams* **14**, 041003 (2011).
- [49] M. G. Billing, J. Conway, E. E. Cowan, J. A. Crittenden, W. Hartung, J. Lanzoni, Y. Li, C. S. Shill, J. P. Sikora, and K. G. Sonnad, Measurement of electron trapping in the Cornell electron storage ring, *Phys. Rev. ST Accel. Beams* **18**, 041001 (2015).
- [50] F. Zimmermann, J. T. Seeman, M. Zolotarev, and W. Stoeffl, Trapped macroparticles in electron storage rings, in *Proceedings of the Particle Accelerator Conference, Dallas, TX, 1995* 1, 517 (IEEE, New York, 1996).
- [51] R. H. Hooverman, Charged particle orbits in a logarithmic potential, *J. Appl. Phys.* **34**, 3505 (1963).
- [52] M. Bassetti and G. Erskine, Closed expression for the electrical field of a two-dimensional Gaussian charge, CERN, CERN-ISR-TH-80-06, ISR-TH-80-06, 1980
- [53] S. Ray and J. Shamanna, Orbits in a central force field: Bounded orbits, <https://arxiv.org/abs/physics/0410149>.